

Kinetics of $O_2(b^1\Sigma_g^+)$ in oxygen RF discharges

A S Kovalev¹, D V Lopaev¹, Yu A Mankelevich¹, N A Popov¹,
T V Rakhimova¹, A Yu Poroykov² and D L Carroll³

¹ Skobel'syn Institute of Nuclear Physics, Moscow State University, Vorobiovy Gory 119992, Russia

² High Technologies, Vorobiovy Gory, MSU 119899, Russia

³ CU Aerospace, 60 Hazelwood Drive, Champaign, IL 61820, USA

Received 10 September 2004, in final form 26 April 2005

Published 1 July 2005

Online at stacks.iop.org/JPhysD/38/2360

Abstract

Studies of the $O_2(b^1\Sigma_g^+)$ kinetics in the afterglow of three RF discharges having different configurations are presented. Experiments with a slow flow velocity transverse capacitive RF discharge were performed and detailed measurements of the spatial evolution of $O_2(b^1\Sigma_g^+)$, $O_2(a^1\Delta_g)$, $O(^3P)$ and flow temperature were taken. Simulations of three different experimental configurations were in good agreement with the data for the spatial decay of $O_2(b^1\Sigma_g^+)$. The simulations also provided reasonable agreement with experimental data for atomic oxygen, $O_2(a^1\Delta_g)$ and temperature, where the data were available. Updated electron impact cross-sections for oxygen dissociation were included in the simulations; this proved critical for proper modelling of the production of atomic oxygen and the subsequent decay of $O_2(b^1\Sigma_g^+)$. At low oxygen atom densities the decay of $O_2(b^1\Sigma_g^+)$ was principally from heterogeneous quenching. For the slow flow velocity experiment, O atom recombination and $O_2(b^1\Sigma_g^+)$ deactivation by the walls play an important role; in the far downstream afterglow region a quasi-stationary $O_2(b^1\Sigma_g^+)$ concentration was found owing to a near-equilibrium between the pooling reaction and losses to the walls for this slow velocity case.

(Some figures in this article are in colour only in the electronic version)

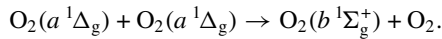
1. Introduction

The problem of creating singlet oxygen (SO) in an electric discharge generator for oxygen–iodine laser pumping has recently attracted heightened attention [1–5]. The development of an effective pumping source of $O_2(a^1\Delta_g)$ using different RF and MW discharge systems [2–5] with a fast flowing gas is of great interest in view of the potential broad abilities, such as possibly providing a large power density in the pumped volume. As is shown by Rakhimova *et al* [4], the α -mode of an RF discharge is one of the most effective for SO excitation. However the amount of energy input into the plasma appeared to be rather small in this discharge mode. The density of atomic oxygen grew with both increasing pressure and energy input so that the three-body process of SO quenching with $O(^3P)$ atoms proposed in [4, 6]

became extremely important. Further, the highest energy inputs provided rather high degrees of oxygen dissociation (>20%) [4, 5] which lead to additional excitation channels of $O_2(a^1\Delta_g)$ owing to cascading from higher metastable states of oxygen molecules, principally from the $O_2(b^1\Sigma_g^+)$ state. In self-sustained discharges, $O_2(b^1\Sigma_g^+)$ molecules are produced primarily from direct electron impact and the quenching of $O(^1D)$ metastable oxygen atoms by O_2 molecules. Thus, the problem of effective pumping of $O_2(a^1\Delta_g)$ in a discharge is rather difficult and requires a detailed experimental–theoretical approach to properly research the different pumping mechanisms. A thorough investigation of the oxygen plasma is necessary to understand the processes occurring in this complex system. These experimental results, coupled with a detailed comparison with theoretical simulations,

should provide important insights into these complex kinetic processes. From this point of view, investigation of the $O_2(b^1\Sigma_g^+)$ molecule kinetics under different experimental conditions should be very useful for testing theoretical models because direct $O_2(b^1\Sigma_g^+)$ concentration measurements are more accurate.

One of the main channels of $O_2(b^1\Sigma_g^+)$ deactivation in a gas-discharge plasma is quenching by atomic oxygen. Therefore, by studying the deactivation dynamics of $O_2(b^1\Sigma_g^+)$ it is possible to pick out the contribution of the given channel and to evaluate the degree of oxygen dissociation. In the afterglow region the production of $O_2(b^1\Sigma_g^+)$ is provided by the pooling reaction:



This reaction provides an initial test for the model and also verification of the absolute intensity calibration of the $O_2(a^1\Delta_g)$ concentration measured in the experiment. The details of the $O_2(b^1\Sigma_g^+)$ kinetics in the post-discharge region are also of interest for its interactions with iodine in particular, to determine the contribution of $O_2(b^1\Sigma_g^+)$ in the I_2 dissociation process with the other products from the electric discharge.

In this work an experimental and theoretical investigation of $O_2(b^1\Sigma_g^+)$ kinetics in an oxygen flow excited by RF discharges with different configurations is presented. Under the investigated conditions it was found that the reaction with atomic oxygen plays an extremely important role in $O_2(b^1\Sigma_g^+)$ quenching. However, good agreement between the experimental and calculated results was possible only after accounting for a more accurate representation of the oxygen dissociation.

2. Experiment

2.1. Transverse capacitive RF discharge

The experimental set-up of the transverse RF discharge is presented in figure 1. The transverse RF discharge was lit in a pure oxygen flow inside a quartz tube having an inner diameter of 14 mm and a length of 1 m. The RF power (up to 250 W at a frequency of 13.56 MHz) from generator '1' was supplied to two parallel plate electrodes of 10 cm length with the flow tube located between the two electrodes. The electrodes were separated by 18 mm. Measurements of the RF system included the amplitudes of the forward and backward waves as well as the voltage across the electrodes, the discharge current and the phase shift between them; these measurements allowed accurate control of the RF power input into the gas. The gas pumping system permitted a gas flow velocity in the tube of up to 15 m s^{-1} at pressures ranging from 1 to 40 Torr. The gas pressure was measured by two capacitance manometers placed on both ends of the discharge tube.

The concentrations of the oxygen molecules in the $a^1\Delta_g$ and $b^1\Sigma_g^+$ metastable states along the gas flow were measured by emission spectroscopy via the absolute intensity emission of the transitions $O_2(a^1\Delta_g, v=0) \rightarrow O_2(X^3\Sigma_g^-, v=0)$ ($\lambda = 1268 \text{ nm}$) and $O_2(b^1\Sigma_g^+, v=0) \rightarrow O_2(X^3\Sigma_g^-, v=0)$ ($\lambda = 762 \text{ nm}$), respectively. The absolute intensity calibrations of the $O_2(a^1\Delta_g)$ and $O_2(b^1\Sigma_g^+)$ concentrations were performed

via chemiluminescence of NO_2 molecules in the afterglow of the RF discharge in a mixture of $N_2 : O_2$, a set of interference filters and a detector for the absolute radiation. The sensitivity of the assembled optical system enabled the measurement of concentrations of $O_2(a^1\Delta_g)$ molecules of $\sim 2\text{--}3 \times 10^{13} \text{ cm}^{-3}$ and $O_2(b^1\Sigma_g^+)$ molecules of $\sim 10^{10} \text{ cm}^{-3}$. The measurement methods for $O_2(a^1\Delta_g)$ and $O_2(b^1\Sigma_g^+)$ in the capacitive RF discharge are described in detail in [4].

The oxygen atoms in the ground state $O(^3P)$ were measured by actinometry with oxygen and argon atoms on the transitions $O(^3P) \rightarrow O(^5S)$ 777 nm and $Ar(2p_1) \rightarrow Ar(1s_2)$ 750 nm, respectively. To use the actinometry technique (discussed in detail in [7]), the O_2 flow was mixed with approximately 5% argon. The first optical channel (figure 1) was used to monitor oxygen atom emission, and the second one was used for argon atom emission. Two identical photomultipliers '8' were used as the detectors. The argon and oxygen atom emission induced by the 13.56 MHz RF discharge was measured in the afterglow region. The actinometric scheme implemented was similar to the technique of laser-induced fluorescence. However, with this actinometric technique the $O(^3P)$ dynamics were illuminated not by a laser, but by another low power ($<1 \text{ W}$) RF discharge '2' with a frequency of 40 MHz. The power of this second discharge was small such that it did not significantly affect the $O(^3P)$ atom density produced by the main 13.56 MHz RF discharge, but it was sufficient for reliable detection of $O(^3P) \rightarrow O(^5S)$ emission. The electrodes of the 40 MHz RF discharge had a length of 1 cm and were placed on the opposite side of the collecting optical fibre on a movable platform '7'. The platform was displaced along the tube axis, which allowed the measurement of the variation of the $O(^3P)$ concentration along the direction of the gas flow after the main 13.56 MHz RF discharge. The actinometric measurement consisted of the signal difference between the I_O/I_{Ar} ratios when the 13.56 MHz RF discharge was switched on and off and thereby the contribution from the dissociative excitation of $O(^3P)$ atoms in the 40 MHz RF discharge to the actinometric signal was fully eliminated. Note that the actinometric technique enables the determination of not just the concentration of $O(^3P)$ atoms, but also the ratio $[O(^3P)]/[O_2^{tot}]$ [7], where $[O_2^{tot}]$ is the initial concentration (before the discharge) of oxygen molecules corresponding to the gas temperature in the studied cross-section of the tube, i.e. it is the O_2 density without taking gas excitation and dissociation in the discharge into account.

As shown in [4], the transverse capacitive RF discharge can operate in three different modes depending on the energy input: (1) the α -mode, where the energy of RF field is input approximately homogeneously into the whole volume of the discharge between the electrodes; (2) the transient mode, where the contribution of γ -processes to the electron generation becomes essential for supporting the discharge structure, but the main energy is still deposited in the inter-electrode region; (3) the surface wave mode, which occurs at large energy inputs and generates a plasma torch with a subsequent transition into a surface-wave discharge that is observed behind the discharge area; in this latter mode the majority of the energy is input by the surface wave outside the volume between the electrodes.

In this work the third mode of the transverse capacitive RF discharge in pure oxygen was selected for studying the

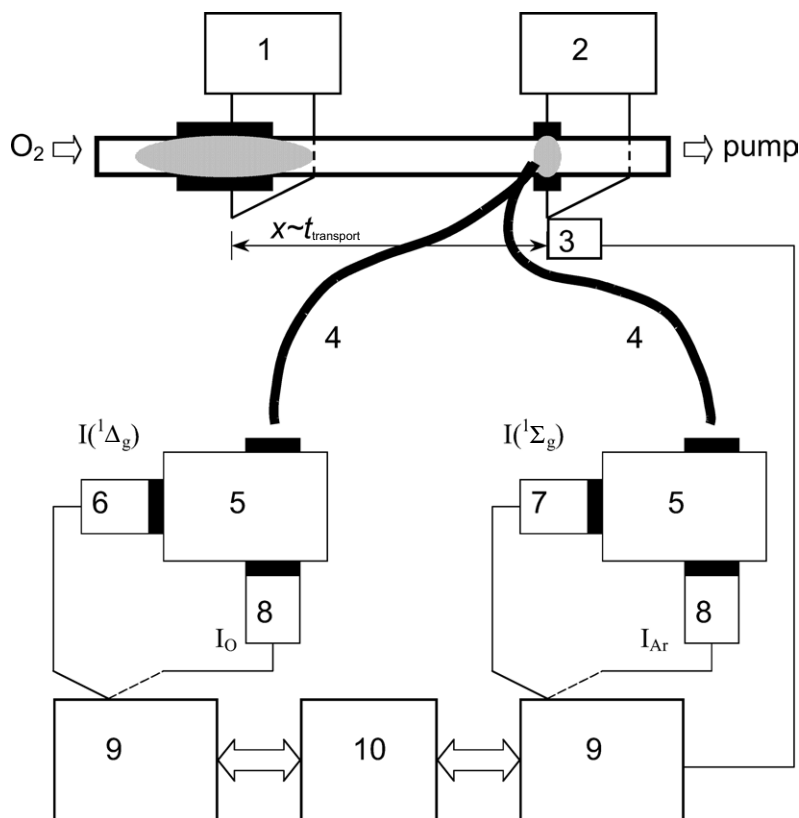


Figure 1. The experimental set-up of the transverse RF discharge. 1—main 13.56 MHz RF discharge (the electrode length of 10 cm), 2—subsidiary 40 MHz RF discharge (the electrode length of 1 cm), 3—measuring system for 40 MHz RF discharge with a translatable fibre optic, 4—double fibre, 5—monochromators, 6—Ge detector cooled by liquid nitrogen, 7—IR sensitive photomultiplier to monitor $O_2(b^1\Sigma_g^+)$ emission, 8—the same photomultipliers to monitor radiation of oxygen and argon atoms: $O(^3P) \rightarrow O(^3S)\lambda = 777$ nm and $Ar(2p_1) \rightarrow Ar(1s_2)\lambda = 750$ nm, 9—lock-in amplifiers, 10—PC.

kinetics of $O_2(b^1\Sigma_g^+)$. As will be clear from the discussion of the experimental results below, the behaviour of $O_2(b^1\Sigma_g^+)$ downstream of the discharge is strongly connected with the kinetics of oxygen atoms and $O_2(a^1\Delta_g)$ molecules. Therefore, it is important to select the discharge mode where the $O_2(a^1\Delta_g)$ and $O(^3P)$ concentrations are high. In accordance with [4] the degree of excitation of $O_2(a^1\Delta_g)$ and oxygen dissociation increases with energy input and reaches a maximum at small pressures of $P < 5$ Torr in the third mode. The experimental data and the results of the calculations for the selected mode of the transverse discharge are presented in section 3.1.

2.2. Longitudinal capacitive RF discharge

The experimental set-up of the longitudinal electrode capacitive RF discharge is shown in figure 2. Two 5 cm wide copper electrodes were placed in a band around the outside of a 4.85 cm (inside diameter) Pyrex flow tube; the electrodes had an inner-to-inner separation of 25 cm. RF power was transferred to the flow through a matching network driven by a 1 kW ENI OEM-12A RF power source at 13.56 MHz. One of the primary measurements on this experiment was a spectrographic determination of $[O_2(b^1\Sigma_g^+)]$ from its emission at 762 nm. A Santa Barbara Instruments Group, Inc. ST-6 CCD camera coupled to a monochromator and a data acquisition computer, and employing KestrelSpec software, provided peak count levels as viewed across the

4.85 cm flow cross-section. Temperature information, T , was calculated from the $O_2(b^1\Sigma_g^+)$ spectra from the intensity of the different rotational energy states. The monochromator was translated along the flow axis to obtain maps of $O_2(b^1\Sigma_g^+)$ and temperature versus position. Qualitative measurements of the $O_2(a^1\Delta_g)$ were also made using an LN₂-cooled intrinsic Germanium Wang detector, filtered by a CVI 1268 nm narrow bandpass filter. Details of these experiments can be found in [3]. Experimental data from [3] for pure oxygen with a molar flow rate of 5 mmol s^{-1} , a pressure of 2 Torr, and 265 W of absorbed power are compared with our modelling predictions for these conditions in section 3.2.

2.3. RF discharge with an inductive coil

The experimental set-up for the inductive RF discharge is shown in figure 3. The instrumentation for this experiment was identical to that described in section 2.2. The only difference between the two setups is that the power was delivered to the oxygen gas through an inductive coil that surrounded the 4.85 cm inside diameter discharge tube. The coil had five turns and was approximately 6.4 cm long in the flow direction. In section 3.3 we compare modelling predictions for experiments that were carried out in pure oxygen at a pressure of 3.4 Torr, a gas flow rate of 7 mmol s^{-1} , and an RF power of 125 W [8].

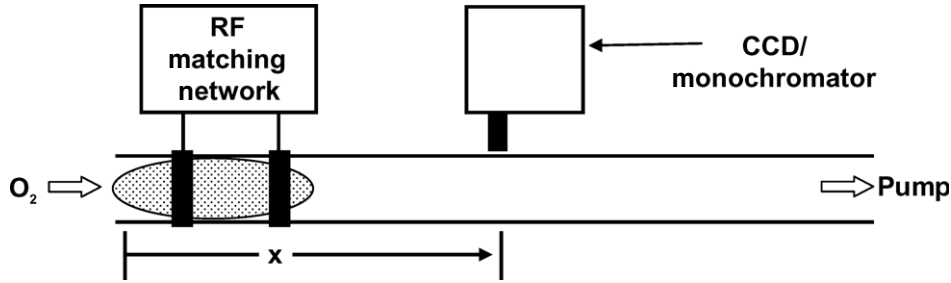


Figure 2. Experimental set-up for the longitudinal capacitive RF discharge experiments. The RF matching network was fed by a 13.56 MHz power supply with the powered electrode upstream and the ground electrode downstream. The CCD/monochromator monitored the $O_2(b^1\Sigma_g^+)$ levels and the gas temperature.

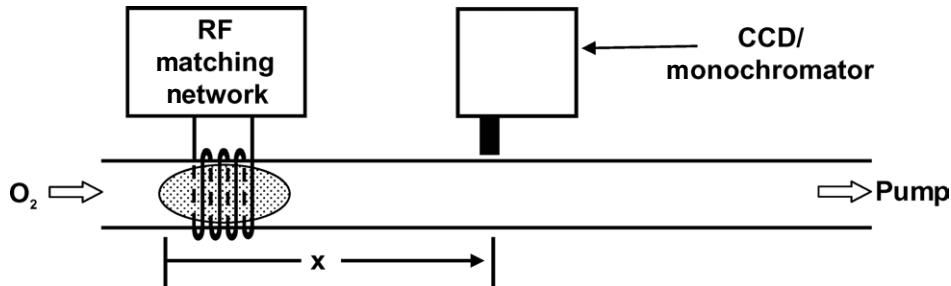


Figure 3. Experimental set-up for the inductive RF discharge experiments. The RF matching network was fed by a 13.56 MHz power supply. The CCD/monochromator monitored the $O_2(b^1\Sigma_g^+)$ levels and the gas temperature.

3. Modelling results

The afterglow region of the transverse capacitive RF discharge was modelled using a zero-dimensional non-stationary kinetic model (zero-dimensional model). For the longitudinal capacitive RF discharge and the RF discharge with an inductive coil, two-dimensional axi-symmetric models, DOIL2Da and DOIL2Db, respectively, were used to simulate the reactive flow with approximated electric field distributions.

The same plasma-chemical mechanism and electron scattering cross-sections developed previously in [6, 9, 10] were used in all three models. The mechanism involves 160 reactions for 18 charged and neutral species in pure oxygen: electrons, negative ions O^- , O_2^- , O_3^- , positive ions O^+ , O_2^+ , O_3^+ , O_4^+ , oxygen molecules in the ground state— $O_2(X^3\Sigma_g^-)$ (hereafter marked as O_2) and the excited vibrational $O_2(v)$, $0 < v < 4$ and electronic states— $O_2(a^1\Delta_g)$, $O_2(b^1\Sigma_g^+)$, O_2^* (the latter is a sum of the Herzberg states), oxygen atoms in the ground $O(^3P)$ and excited $O(^1D)$ states, as well as ozone molecules O_3 . The main processes involved in the kinetic scheme are presented in detail in [6, 9].

In the afterglow of the transverse capacitive RF discharge, the gas temperature, oxygen atoms, $O_2(a^1\Delta_g)$ and $O_2(b^1\Sigma_g^+)$ molecules were measured simultaneously and we have used the semi-empirical zero-dimensional model to check the self-consistency of these experimental data with the evolution of $O_2(b^1\Sigma_g^+)$. In the zero-dimensional model of the afterglow region, non-stationary conservation equations were solved only for the neutral species; initial conditions for the afterglow region were taken from radially averaged experimental data on species concentrations and gas temperature at the end of the plasma region. It is assumed that it is possible to correlate the calculated temporal evolution of the species

concentrations in the zero-dimensional model to the radially averaged experimental spatial concentrations. The correlation between time scale and axial position was established using the experimental flow rate and the gas temperature profile, i.e. the time evolution was converted to a spatial evolution via a velocity profile determined from the measured flow rate and temperature profile.

The developed two-dimensional cylindrical (r, z) models DOIL2Da and DOIL2Db include non-stationary neutral and charged species conservation equations:

$$\frac{\partial n_i(r, z)}{\partial t} = S_i - L_i n_i + Q_i,$$

where n_i is i th species concentration, S and L_n are production and loss terms owing to plasma-chemical reactions and Q is the species transport term. For neutral species the model includes axial transfer with flow velocity $v(r, z)$ as well as radial and axial diffusion transfer:

$$Q_i = -\frac{\partial(n_i v)}{\partial z} + \nabla \cdot \left(D_i N \nabla \left(\frac{n_i}{N} \right) \right),$$

where N is local total gas concentration, D_i are the binary diffusion coefficients of different species in O_2 taken as $D_i = a \cdot T^{1.5}/P$; T and P are gas temperature and pressure, and $a = 0.045$ [$\text{cm}^2 \text{Torr} (\text{s K}^{1.5})^{-1}$] for atomic oxygen species, $a = 0.03$ for molecular species and $a = 0.025$ for O_3 . More complex transport terms Q of charged species include only radial diffusion and drift [9]. The gas temperature distribution $T(r, z)$ in our almost constant pressure conditions was calculated from the energy conservation equation of reactive flow with radial and axial thermal conductivity terms and Joule heating [11].

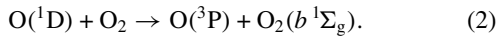
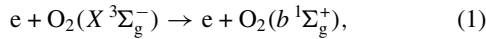
The electron energy distribution function (EEDF), electron temperature and electron-particle reaction rate

coefficients are recalculated in a local field approximation by solving the Boltzmann equation in a two-term approach [6] at each time step and spatial grid point for the current mixture composition.

Such recalculation of EEDF rather than the more common preliminary calculation of rate coefficients is important for this highly excited and non-uniform plasma. In calculating the EEDF we took into account the electron scattering for the ground state oxygen molecules, the excited $O_2(a^1\Delta_g)$ and $O_2(b^1\Sigma_g^+)$ molecules as well as the $O(^3P)$ oxygen atoms. The excitation and de-excitation of molecular O_2 vibrational levels by electron impact and processes of VT-relaxation and VV-exchange were also taken into account in these calculations.

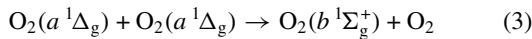
For the two-dimensional models the radial gas flow velocity distribution is assumed to be an established laminar flow $v(r, z) = 2v_0(z)(1 - r^2/R^2)$, where $v_0(z)$ is the mean flow velocity determined from the experimental mass flow F , $F = 2\pi \int_0^R \rho(r, z)v(r, z)dr$, R is the tube radius and ρ is the gas density. The only difference between the two two-dimensional models was how the electrical energy was transferred into the flow, i.e. in the discharge region. The methods of power dissipation calculation will be described in sections 3.2 and 3.3.

The main processes of $O_2(b^1\Sigma_g^+)$ production and loss for our discharge conditions are assumed to be the following. As shown in [4–6, 9, 12], in the gas-discharge plasma there are two main channels of $O_2(b^1\Sigma_g^+)$ excitation:



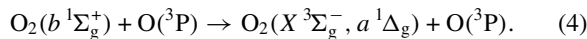
Cascading processes from the higher (Herzberg) electronic states of the O_2 molecules contribute to a lesser degree in populating the $O_2(b^1\Sigma_g^+)$ state.

In the afterglow region a major source of $O_2(b^1\Sigma_g^+)$ comes from the pooling reaction:



with a rate constant $k_3 = 2 \times 10^{-17} \text{ cm}^3 \text{ s}^{-1}$ at $T = 295 \text{ K}$ [13]. As shown in [14], the rate constant k_3 grows strongly with increasing temperature such that an accurate calculation of the gas temperature dynamics is necessary for correctly describing the $O_2(b^1\Sigma_g^+)$ behaviour in the afterglow, especially for the slow flow velocity case discussed below in section 3.1.

Deactivation of $O_2(b^1\Sigma_g^+)$ both in the discharge and in the afterglow occurs mostly from $O(^3P)$ atoms and ozone molecules; also some deactivation occurs on the wall surface. The most important deactivation channel is $O_2(b^1\Sigma_g^+)$ quenching by oxygen atoms [15]:



The generally used value for the rate constant of reaction (4) is $k_4 = (8 \pm 2) \times 10^{-14} \text{ cm}^3 \text{ s}^{-1}$, with a branching ratio of 0.9 to the $a^1\Delta_g$ state, which was directly measured only in [16]. There are many indirect data indicating that this rate constant can be higher so that the value from [16] can be considered a lower bound. Since at present there are no other direct data

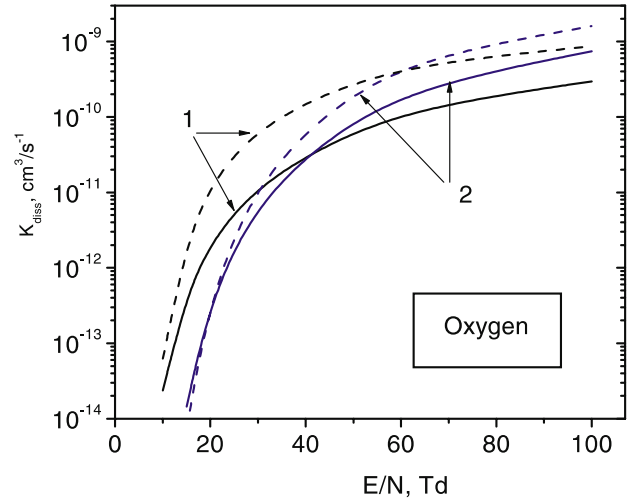
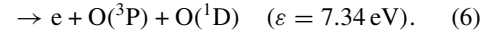
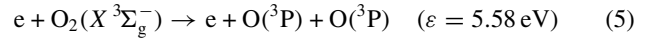


Figure 4. The dissociation rate constants of O_2 for reactions (5) and (6), calculated using our self-consistent cross-section set (solid curves 1 and 2, respectively) and cross-section set from [20] (dashed curves 1 and 2, respectively), as a function of E/N .

for this reaction we use the value that is recommended in [17], i.e. $k_4 = (8 \pm 2) \times 10^{-14} \text{ cm}^3 \text{ s}^{-1}$.

The dissociation of O_2 in the discharge occurs by direct electron impact as follows:



In reality slightly more energy is required owing to the Frank–Condon corridor. The dissociation via channel (5) runs through unbounded Herzberg states. The oxygen dissociation via channel (6) occurs through the excitation of the $O_2(B^3\Sigma_u^-)$ state continuum. Simulations of different oxygen discharges [7, 10, 18, 19] indicated that it was necessary to modify the total dissociation cross-sections presented in [20] and to reduce the contribution from process (5). Experimental data from [22] directly show that there is a lower contribution from process (5) and a reduction by approximately a factor of two for the peak of the total dissociation cross-section. This modified cross-section set was verified by comparison with a large set of experimental data [7, 10, 18, 19]. In this paper, we used these modified electron impact cross-sections for oxygen dissociation channels (5) and (6) rather than those of [20].

Figure 4 shows the O_2 dissociation rate constants as a function of E/N for reactions (5) and (6) calculated using our cross-section set (solid curves 1 and 2, respectively) and the cross-sections from [20] (dashed curves 1 and 2, respectively). As seen in figure 4, in the range of $E/N \sim 25\text{--}70 \text{ Td}$, typical of all the experimental conditions considered reported herein, the total dissociation rate coefficient for our cross-sections is lower by about a factor of approximately 3 as compared with the cross-sections from [20]. The rate coefficient for process (5) is lower by 3.5–6 times, and the most significant deviation occurs at a reduced field E/N of around 30 Td.

For comparison we ran our two-dimensional model of the longitudinal RF discharge with an inductive coil (section 3.3), at an $E/N = 23 \text{ Td}$, with dissociation cross-sections from [20] and with our updated cross-section set. The calculation with cross-sections from [21] resulted in a

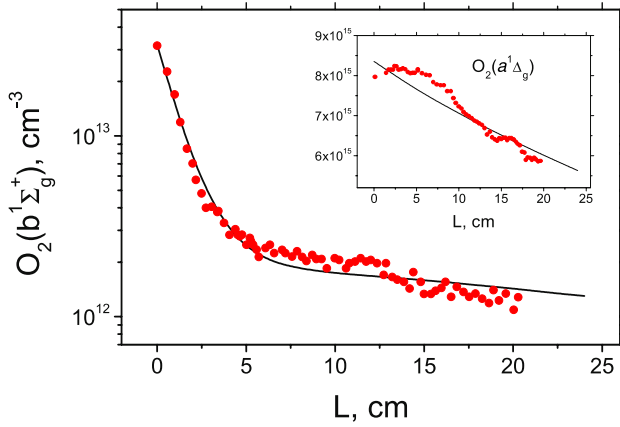


Figure 5. The evolution of the $O_2(b^1\Sigma_g^+)$ density after the transverse capacitive RF discharge. The inset in this figure shows the evolution of the $O_2(a^1\Delta_g)$ density. The discharge tube diameter—1.4 cm, pressure of O_2 —4 Torr, gas velocity— 6.3 m s^{-1} , RF power—120 W. ‘0’ on the ‘X’ axis corresponds to the end of electrodes of the 13.56 MHz RF discharge. The solid lines are the zero-dimensional model predictions.

higher total dissociation rate (approximately 3.5 times higher rate) and an overall higher atomic oxygen concentration in the discharge zone (approximately 1.5 times higher concentration) than the calculation with our updated (reduced) dissociation cross-sections. If a global zero-dimensional model were used for these conditions the $O(^3P)$ concentration would be overestimated by approximately 3.5 times using cross-sections from [20]. However, our two-dimensional simulation accounts for non-uniform radial and axial $O(^3P)$ distributions as well as transport losses, which results in a lower overall scaling factor of approximately 1.5 times higher concentration than the corresponding calculation with the updated dissociation cross-sections.

3.1. Transverse capacitive RF discharge

In this section we present modelling results of the dynamics of the main components of the oxygen gas flow after exiting the transverse RF discharge described above. As already noted, the dynamics of the $O_2(a^1\Delta_g)$, $O_2(b^1\Sigma_g^+)$, $O(^3P)$ and gas temperature in the post-discharge region were measured in these experiments. The studies were carried out in a quartz tube of radius $R = 0.7 \text{ cm}$ at a pressure of 4 Torr. The flow velocity of the gas entering the discharge is estimated to be 6.3 m s^{-1} . Under these conditions the influence of the heterogeneous loss of the particles on the tube walls is expected to be significant and therefore the choice of values of the corresponding accommodation coefficients γ_a , γ_b is important.

The evolution of the population of the $O_2(b^1\Sigma_g^+)$ state after the transverse RF discharge is presented in figure 5. The inset in this figure shows the evolution of the $O_2(a^1\Delta_g)$ concentration. Note that the experimental $O_2(a^1\Delta_g)$ concentration stays relatively constant at the beginning of the afterglow region (in the first 5 cm), whereas the model predicts a monotonic decay; the reason for this discrepancy is unknown but could be a result of the flow transfer of $O_2(a^1\Delta_g)$ from the discharge that is not included in the zero-dimensional model, e.g. the $\nabla(v \cdot [O_2(a^1\Delta_g)])$ term with declining flow velocity v

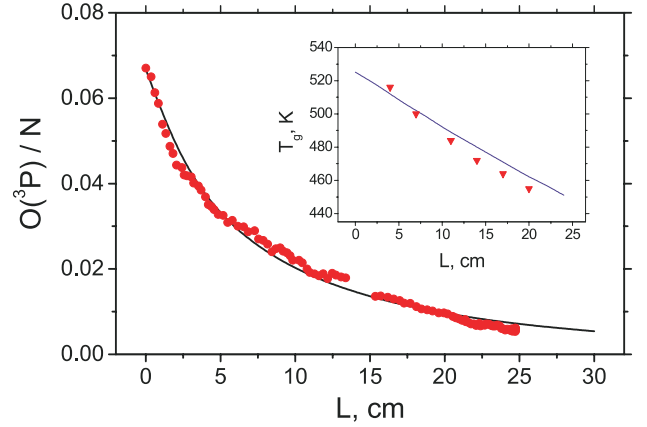


Figure 6. The post-discharge dynamics of the degree of oxygen dissociation $O(^3P)/N$ (N —total gas density at the local temperature) for the same conditions as in figure 5. The inset presents the evolution of the gas temperature. The solid lines are the zero-dimensional model predictions.

in the afterglow. Figure 6 shows the post-discharge dynamics of the degree of oxygen dissociation $O(^3P)/N$ (where N is the total gas density at the temperature of the gas measured at that location) at the same conditions as in figure 5. The inset in figure 6 presents the evolution of the gas temperature. The experimentally measured values of the $O_2(a^1\Delta_g)$ and $O_2(b^1\Sigma_g^+)$ densities, the gas temperature and the degree of oxygen dissociation at the exit of the discharge (the beginning of the afterglow region) were used as input parameters for the modelling calculations. For the $O(^3P)$ atom wall loss probability γ_0 we used an expression extracted from fitting previous experimental data obtained for an uncooled quartz tube in an oxygen dc discharge [22, 23],

$$\gamma_0 = 0.0015 \left(0.5 + 1.7A \frac{[O(^3P)]}{4 \times 10^{15}} \right), \quad (7)$$

where $A = 1$ at $P \leq 5$ Torr and $A = 5/P$ at $P > 5$ Torr.

The main channel of $O_2(a^1\Delta_g)$ loss under these slow flow conditions is from quenching on the tube walls. The calculation with a loss probability of $O_2(a^1\Delta_g)\gamma_a = 4 \times 10^{-4}$ [24, 25] adequately describes the experimental data (see inset in figure 5). As is seen in figure 5, there are two stages in the evolution (decay) of $O_2(b^1\Sigma_g^+)$ concentration having very different characteristic times. In the first stage, both loss terms of $O_2(b^1\Sigma_g^+)$ —quenching by oxygen atoms and on the tube walls—are important. A separate series of measurements of the $O_2(b^1\Sigma_g^+)$ loss probabilities γ_b on the quartz tube wall were carried out in [24]. It was found that γ_b depends on the plasma conditions and there is a substantial difference in γ_b for the plasma and afterglow regions. A typical value of γ_b in the plasma region was $\gamma_b = 0.1$. In the afterglow region, γ_b was in the range 0.015–0.025 and γ_b was found to be almost independent of temperature for wall temperatures of 300–400 K. In our simulations, $\gamma_b = 0.016$ was used for the afterglow region. The concentration of ozone molecules was predicted to be small because of the low pressure and high gas temperature, and consequently quenching by ozone was insignificant. Note that calculations with cross-sections from [20] would result in significantly

higher O atom concentrations and consequently a significant increase in the quenching of $O_2(b^1\Sigma_g^+)$ through process (4); the measured quenching rate is not consistent with O atom concentrations predicted using cross-sections from [20] but is consistent with O atom concentrations predicted using the updated cross-sections for processes (5) and (6). In the second stage, the quenching rate of $O_2(b^1\Sigma_g^+)$ is determined by a balance between wall quenching (note that the quenching due to oxygen atoms drops significantly as the atoms are recombined on the walls, figure 6) and the production of $O_2(b^1\Sigma_g^+)$ from the pooling reaction (3). Therefore, the decay rate of the $O_2(b^1\Sigma_g^+)$ concentration decreases in the second stage because the pooling source term becomes comparable to the reduced quenching term. Since the level of the $O_2(b^1\Sigma_g^+)$ concentration is determined here only by the rate of quenching and the pooling source term, the $O_2(b^1\Sigma_g^+)$ and gas temperature measurements together with modelling of the $O_2(b^1\Sigma_g^+)$ dynamics in the second stage provide us with an additional method to check the absolute intensity calibration of the $O_2(a^1\Delta_g)$ measurement scheme, i.e. the $O_2(a^1\Delta_g)$ calibration was consistent with the magnitude of the source term from reaction (3) and the measured decay of $O_2(b^1\Sigma_g^+)$ in the second stage.

3.2. Longitudinal capacitive RF discharge

Complete modelling of the structure of the longitudinal capacitive RF discharge with a rather remote grounded electrode depends on the construction (geometry and hardware) of the experimental set-up. The distribution of the electrostatic fields depends strongly on the surrounding metallic objects, screening grids, etc that are placed near the discharge. For the conditions of the given experiment the power supplied to the ‘powered’ electrode should be distributed relative to this electrode almost symmetrically upstream and downstream. However, by varying the construction of the experimental set-up, it is possible to change the power distribution. Thus, the distribution of electrical fields in this experiment should be determined from the solution of the three-dimensional Poisson equation while taking into account the construction of the studied discharge.

Since it is difficult to solve this problem for the general case as well as to correctly take into account all the geometric and hardware features, we have chosen to use a modified version of the two-dimensional model from [5], DOIL2Da, for modelling the longitudinal capacitive RF discharge.

Sustained reduced electric fields $(E/N)_{\text{eff}}$ are assumed to be radially uniform and their axial behaviour was determined from the following equation for the radially averaged power flux $W(z)$ upstream and downstream from the powered electrode [26, 27]:

$$\frac{dW}{dz} = -\alpha W(z). \quad (8)$$

Here α is a coefficient of electromagnetic wave absorption. The approach used is based on an analytic expression for $\alpha(z)$ with the following assumptions:

$$\omega \ll \nu \ll \frac{\omega_p^2}{\omega}. \quad (9)$$

(ω —wave frequency, ν —electron collision frequency, ω_p —plasma frequency) and weak radial non-uniformity. A symmetric relation $W(z = z_0) = 0.5W_0$ at the centre of the ‘powered’ electrode z_0 was used as a boundary condition. For a given total input power W_0 and known function $\alpha(z)$ [26, 27], the length of the plasma region and $(E/N)_{\text{eff}}(z)$ is determined automatically by solving equation (8). Then the reduced electric field E/N can be calculated from the equation:

$$\frac{dW}{dz} = 2\pi \left(\frac{E}{N}\right)_{\text{eff}}^2 \int_0^R \sigma_e(r) N^2(r) r dr, \quad (10)$$

where

$$\left(\frac{E}{N}\right)_{\text{eff}} = \frac{Ev\langle\sigma u\rangle}{\nu^2 + \omega^2}, \quad (11)$$

where σ is the total electron collision cross-section, u the electron velocity, $\sigma_e(r)$ the electron conductivity and $N(r)$ the gas concentration. Radial non-uniformity of E/N deals with radial dependence of the gas temperature and thus $N(r)$. This approach fails to correctly take into account the edge effects upstream, but we believe that the influence of these factors will not be very significant for the total absorbed power.

The model’s equations are numerically integrated until a steady state regime is reached. As a result, radial and axial distributions of the gas temperature, the gas velocity, the species concentrations, and the axial $(E/N)_{\text{eff}}$ profile have been obtained. Because of our simplified assumption of the radial uniformity of $(E/N)_{\text{eff}}$, we do not lay special emphasis on predicting a realistic description of the discharge parameters radial profiles. Thus, all presented results are radially averaged.

The calculated results for the longitudinal capacitive RF discharge in pure oxygen with a tube of diameter 4.85 cm at a pressure of 2 Torr, gas flow rate of 5 mmol s^{-1} , and absorbed power of 265 W are presented in figures 7–9. The experimental temperature and scaled $O_2(b^1\Sigma_g^+)$ data are presented for comparison in figures 8 and 9 (note that the $O_2(b^1\Sigma_g^+)$ data were scaled because no absolute intensity calibration was available for this data set). The calculated axial distributions of charged particle densities averaged over the discharge tube cross-section are shown in figure 7. As seen from the simulation, the RF power applied to the ‘powered’ electrode is absorbed over distances of the order of 20 cm upstream and downstream from this electrode so that the discharge exists in a recombination mode. The averaged electron density near the ‘powered’ electrode is approximately $1.7 \times 10^{10} \text{ cm}^{-3}$. Some asymmetry in the discharge relative to the ‘powered’ electrode is connected with a small density of active particles that actively ‘destroy’ negative ions through associative detachment reactions, which leads to a high plasma electronegativity in the upstream discharge zone. Therefore, the electron temperature upstream appears to have a rather high $T_e \cong 3 \text{ eV}$ ($E/N \cong 85 \text{ Td}$), which is significantly higher than the corresponding values in the discharge downstream.

The experimental data and calculated gas temperature T_g as a function of distance along the flow axis are presented in figure 8. The position of the electrodes are marked by dark squares. Generally good agreement is observed in both the distribution (profile and location of the peak temperature) and the absolute value of T_g . The difference in the maximum value is

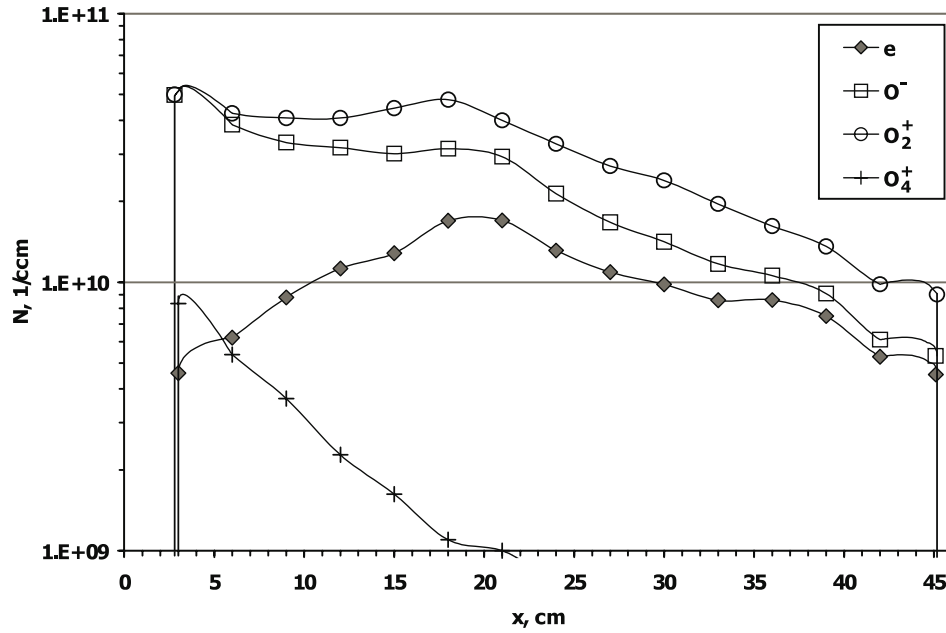


Figure 7. The calculated axial distributions of the charged particle densities averaged across the discharge tube cross-section in the longitudinal capacitive RF discharge. Diameter of discharge tube—4.85 cm, pressure of O_2 —2 Torr, gas flow— 5 mmol s^{-1} , RF power—265 W.

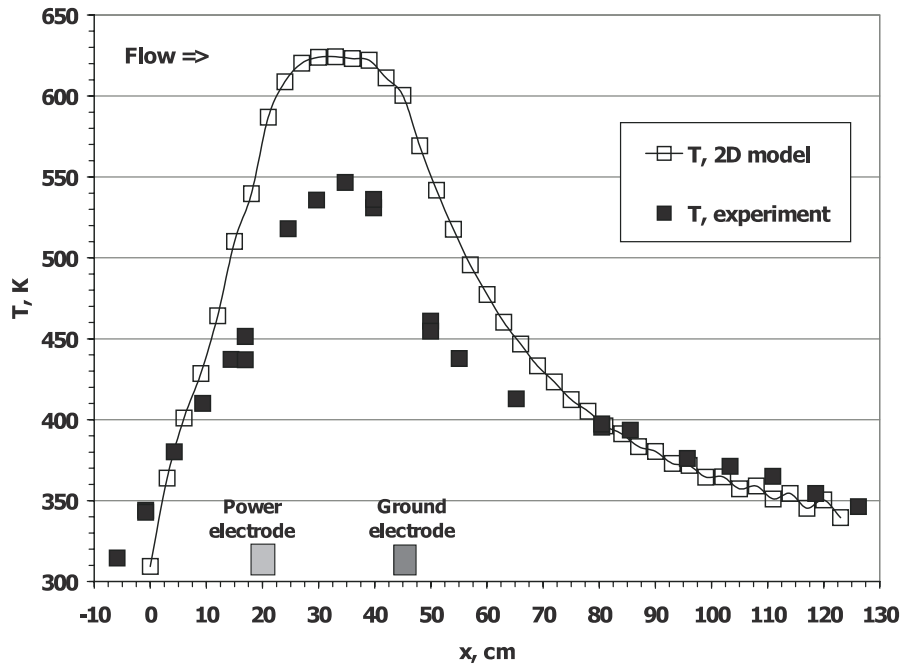


Figure 8. The experimental (■) and calculated (—□—) spatial distribution of the gas temperature T_g in the longitudinal capacitive RF discharge for the conditions in figure 7.

less than 15%. The experimental and calculated axial distributions of $O_2(b^1\Sigma_g^+)$ density as well as the computed distribution of atomic oxygen concentration are shown in figure 9. There is also very reasonable agreement between the experimental and simulated results of the spatial evolution of the $O_2(b^1\Sigma_g^+)$ concentration. Note that the calculated values of $O_2(b^1\Sigma_g^+)$ concentration and gas temperature presented in figures 8 and 9 were averaged over that part of the tube volume from which the $O_2(b^1\Sigma_g^+)$ emission data were collected; in other words, because the data were sampled across the flow tube with a

2 cm diameter light collection optic, the numerical results were averaged across the tube through a 2 cm viewing area for a more accurate comparison with the experimental data.

A recent O atom titration with NO_2 was run in [28] for a 5 mmol s^{-1} pure oxygen flow at 2.3 Torr with an absorbed power of approximately 265 W, i.e. for approximately the same conditions as discussed in this section. This measurement gave an atomic oxygen yield of 2.8% when the NO_2 injection point was 58.4 cm downstream of the exit of the discharge or approximately at a position of 100 cm in figure 9. If we take

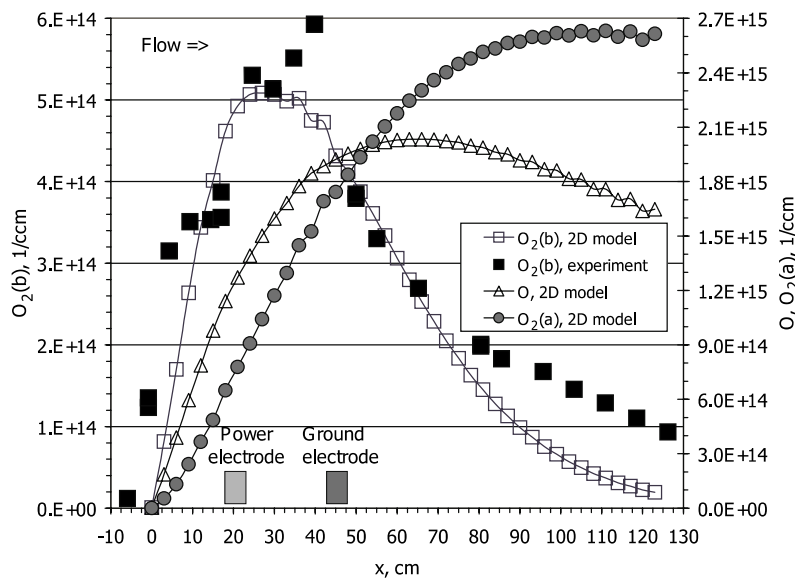


Figure 9. The experimental (■) and calculated (—□—) spatial distributions of the $O_2(b\ ^1\Sigma_g^+)$ density, the calculated $O_2(a\ ^1\Delta_g)$ distribution (—●—) and the calculated distribution (—△—) of the $O(^3P)$ atom concentration in the longitudinal capacitive RF discharge for the conditions in figure 7.

the temperature of approximately 370 K from figure 8, a 2.8% O-atom yield in a 2.3 Torr flow of pure oxygen corresponds to a number density of 1.71×10^{15} molecules cc^{-1} ; the simulation is in close agreement with this data point (figure 9).

3.3. Longitudinal inductive RF discharge

In these experiments the RF power was coupled into the gas flow by an inductive ‘coil’. It should be noted that the structure of this discharge is somewhat different from the longitudinal capacitive discharge considered above. For this configuration the discharge structure of the space inside the ‘coil’ will be non-uniform principally because of a radially (and axially) dependent electric field with a field strength of zero along the centre of the flow tube. Thus, both inhomogeneous models described above for the modelling of transverse and longitudinal capacitive RF discharges [4] are not adequate for describing the experimental results of this inductive RF discharge. The slow decay rate of the experimentally measured $O_2(b\ ^1\Sigma_g^+)$ concentration [8] in the downstream post-discharge region suggests a low density of the quenching species (in this case the O atoms). A low O atom density could be a result of rather low values of the electrical field. At a discharge power of 125 W and gas flow rate of $7\ \text{mmol s}^{-1}$ (which corresponds to an energy input of $W \cong 0.18\ \text{eV mol}^{-1}$), the portion of the energy deposited into $O_2(b\ ^1\Sigma_g^+)$ excitation appears to be approximately 15% for the experimental $O_2(b\ ^1\Sigma_g^+)$ mole fraction $X(O_2(b\ ^1\Sigma_g^+)) \sim 0.02$. EEDF calculations at a constant E/N show that such a yield into the $O_2(b\ ^1\Sigma_g^+)$ state is possible only for $E/N < 20\ \text{Td}$ and indirectly indicates that the value of E/N in the central part of the discharge volume is actually relatively small [8].

In order to somehow simulate the features of the inductive RF discharge with a coil, the DOIL2Da model was modified by assuming that the majority of the RF power is dissipated inside the coil area with some effective field E/N . Thus, in

this non-self-consistent DOIL2Db model an artificial source of electrons was used to fit the total input power for a given constant E/N , which was too low to provide self-sustained electron production. In fact, to provide a high efficiency of $O_2(b\ ^1\Sigma_g^+)$ excitation it is necessary to have an E/N lower than that required to support a self-sustained discharge. Therefore the source of ionization in this zone (which simplistically models the flux of charged particles from near-electrode layers) was taken to be a constant, and its value was chosen from a condition that results in the experimentally measured power. Of course, the calculations with such an approximation do not describe the excitation in real inhomogeneous fields but only the excitation in some effective field.

Calculations of the axial distributions of $O_2(b\ ^1\Sigma_g^+)$, $O_2(a\ ^1\Delta_g)$ and atomic oxygen concentrations in the discharge with an inductive RF coil at a pressure of 3.4 Torr and an applied power of 125 W with an $E/N = 23\ \text{Td}$ are presented in figure 10. The value of $E/N = 23\ \text{Td}$ used in these calculations agrees reasonably well with the measured value of $E/N \cong 15\text{--}20\ \text{Td}$ [8]. The experimental data are also presented, but note that they have been scaled by a factor of 0.25 (discussed below). The spatial position of the ‘coil’ is marked by a dark rectangle. As seen in figure 10, there is satisfactory agreement between the measured and calculated results of the decay dynamics of the $O_2(b\ ^1\Sigma_g^+)$ density. This agreement appears to be possible only because of a low degree of O_2 dissociation at this E/N value. For the low degree of dissociation under these discharge conditions, quenching of $O_2(b\ ^1\Sigma_g^+)$ in the afterglow region is determined mainly by heterogeneous processes at the tube wall. In this case, the quenching rate of $O_2(b\ ^1\Sigma_g^+)$ depends on the diffusion transfer of $O_2(b\ ^1\Sigma_g^+)$ to the flow tube wall and the loss probability at the wall.

However, note that the absolute concentration of $O_2(b\ ^1\Sigma_g^+)$ in the calculation is lower than the experimentally measured values (the scaling factor of 0.25). We carried out

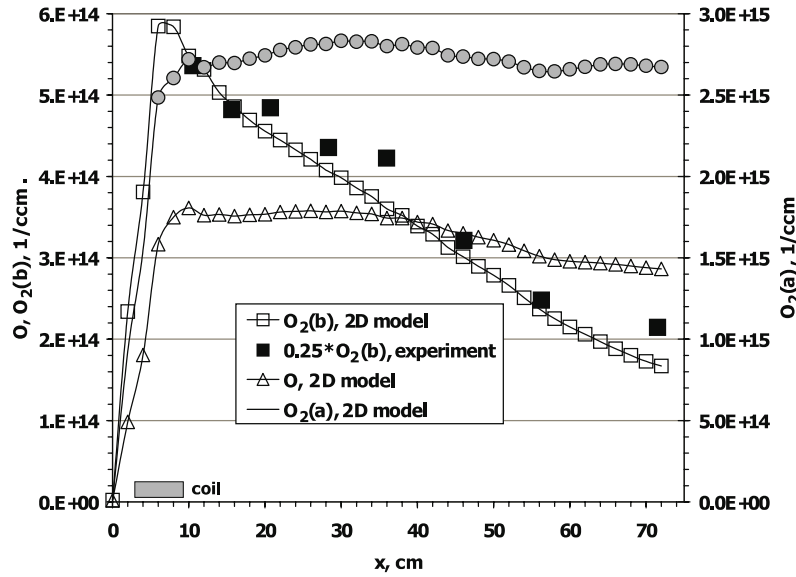


Figure 10. The spatial distributions of $O_2(b^1\Sigma_g^+)$, $O_2(a^1\Delta_g)$ and atomic oxygen concentrations in the inductive discharge case with a 'coil'. Solid squares—experimental $O_2(b^1\Sigma_g^+)$ data, lines—simulation at $E/N = 23$ Td. Diameter of discharge tube—4.85 cm, pressure of O_2 —3.4 Torr, gas flow— 7 mmol s^{-1} , RF power—125 W.

the calculation for different electric fields (values of E/N) to obtain the best agreement with the experimental distribution of the $O_2(b^1\Sigma_g^+)$ concentration data rather than the absolute magnitude. It should be noted that model calculations made with an E/N of 10 Td, corresponding to the maximum of energy efficiency of $O_2(b^1\Sigma_g^+)$ excitation [6], increase the scaling factor to 0.5 but still fail to obtain the density of $O_2(b^1\Sigma_g^+)$ measured in the experiments (the scaling factor of 0.25). Discussions with the author [29] indicated that the absolute intensity calibrations may have been too high by approximately a factor of two; if that is the case then predictions of the $O_2(b^1\Sigma_g^+)$ excitation would be in better agreement with the $O_2(b^1\Sigma_g^+)$ measurements. However, it is not physically reasonable that this discharge would operate at the optimal E/N ; therefore, we do not believe that the 10 Td calculation is reasonable for this case and have chosen to present the 23 Td simulation as being more realistic. A more complete set of high velocity flow data would help to resolve the differences between the existing model and experiment.

4. Conclusions

Studies of the $O_2(b^1\Sigma_g^+)$ kinetics in the afterglow of three RF discharges having different configurations are presented. In a slow flow velocity transverse capacitive RF discharge it was observed that the deactivation of $O_2(b^1\Sigma_g^+)$ by atomic oxygen and tube walls has the greatest influence on the kinetics of this state at these flow conditions and for pressures ≤ 4 Torr. Because our $O_2(b^1\Sigma_g^+)$ diagnostic has a high sensitivity to the $O_2(b^1\Sigma_g^+)$ concentration (of $\sim 10^{10} \text{ cm}^{-3}$), we were able to make accurate spatial measurements of the evolution of the $O_2(b^1\Sigma_g^+)$ state; this allowed us to experimentally observe a transition to a quasi-stationary $O_2(b^1\Sigma_g^+)$ concentration owing to a near-equilibrium between the pooling reaction (3) and losses to the wall that was confirmed by modelling simulations. This also provided an additional check on the

$O_2(a^1\Delta_g)$ concentration measurement scheme and the result was consistent with the $O_2(a^1\Delta_g)$ calibration.

The evolution of $O_2(b^1\Sigma_g^+)$ in an oxygen flow excited by a longitudinal capacitive RF discharge in a wide quartz tube with a diameter of 4.85 cm was investigated. It was found that in this fast flowing case, quenching of $O_2(b^1\Sigma_g^+)$ by oxygen atoms is the main channel of $O_2(b^1\Sigma_g^+)$ deactivation (consistent with conclusions drawn in [15] for similar fast flow conditions). Thus, the accurate simulation of oxygen dissociation by electron impact is critical to adequately describe the evolution of the $O_2(b^1\Sigma_g^+)$ density in both the discharge and in the post-discharge region. The fact that the predicted $O_2(b^1\Sigma_g^+)$ evolution and atomic oxygen concentrations in the post-discharge region agreed well with the experimental data suggests that the excitation cross-sections used in this work are reasonable.

A simulation of the $O_2(b^1\Sigma_g^+)$ evolution in fast flowing oxygen excited by an inductive RF discharge showed that the kinetic model correctly reproduced the decay of $O_2(b^1\Sigma_g^+)$ observed in the experiment. While the decay of $O_2(b^1\Sigma_g^+)$ was well modelled, the absolute concentration of $O_2(b^1\Sigma_g^+)$ in the calculation was noticeably lower than measured. It should be noted that even with a value of E/N corresponding to the maximum $O_2(b^1\Sigma_g^+)$ excitation the model fails to obtain the reported density of $O_2(b^1\Sigma_g^+)$. The reason for the differences is not presently known, but a more complete set of high velocity flow data would help to resolve the differences between the existing model and experiment.

References

- [1] Napartovich A P, Deryugin A A and Kochetov I V 2001 *J. Phys. D: Appl. Phys.* **34** 1827
- [2] Fujii H *et al* 2000 *Proc. SPIE* **4065** 818
- [3] Carroll D L, King D M, Verdeyen J T, Woodard B, Zimmerman J, Skorski L and Solomon W C 2003 *34th*

- Plasmadynamics and Lasers Conf. (Orlando, 2003)* AIAA 2003-4029
- [4] Rakhimova T V, Kovalev A S, Rakhimov A T, Klopovsky K S, Lopaev D V, Mankelevich Yu A, Proshina O V, Braginsky O V and Vasilieva A N 2003 *34th Plasmadynamics and Lasers Conf. (Orlando, 2003)* AIAA 2003-4306
- [5] Savin Yu V et al 2004 *J. Phys. D: Appl. Phys.* **37** 3121–8
- [6] Vasiljeva A N, Klopovsky K S, Kovalev A S, Lopaev D V, Mankelevich Yu A, Popov N A, Rakhimov A T, Rakhimova T V and Vasilieva A N 2004 *J. Phys. D: Appl. Phys.* **37** 2455–68
- [7] Ivanov V V, Klopovskiy K S, Lopaev D V, Rakhimov A T and Rakhimova T V 2000 *Plasma Phys. Rep.* **26** 980–90
- [8] Verdeyen J T, King D M, Carroll D L and Solomon W C 2002 *Proc. 3rd Conf. of the Gas and Chem. Lasers (San Jose, 2002)* pp 154–60
- [9] Ivanov V V, Klopovsky K S, Lopaev D V, Proshina O V, Rakhimov A T and Rakhimova T V 2000 Institute of Nuclear Physics MSU Report No 2000-16/620 (Moscow)
- [10] Zakharov A I, Klopovsky K S, Osipov A P, Popov A M, Popovicheva O B, Rakhimova T V, Samorodov V A and Sokolov A P 1988 *Fiz. Plasmy* **14** 327–33 (in Russian)
- [11] Raizer Yu P 1987 *Physics of Gas Discharges* (Moscow: Nauka)
- [12] Stafford D S and Kushner M J 2004 *J. Appl. Phys.* **96** 2451
- [13] Derwent R G and Thrush B A 1971 *Trans. Faraday Soc.* **67** 2036
- [14] Heidner R F III, Gardner C E, El-Sayed T M, Segal G I and Kasper J V V 1981 *J. Chem. Phys.* **74** 5618
- [15] Carroll D L, Verdeyen J T, King D M, Woodard B S, Skorski L W, Zimmerman J W and Solomon W C 2003 *IEEE J. Quantum Electron.* **39** 1150
- [16] Slanger T G and Black G 1979 *J. Chem. Phys.* **70** 3434
- [17] Baulch D L, Cox R A, Hampson R F and Kerr J A 1984 *J. Phys. Chem. Ref. Data* **13** 1259
- [18] Ivanov V V, Klopovskiy K S, Lopaev D V, Rakhimov A T and Rakhimova T V 2000 *Plasma Phys. Rep.* **26** 972–9
- [19] Ivanov V V, Klopovskiy K S, Lopaev D V, Rakhimov A T and Rakhimova T V 1999 *IEEE Trans. Plasma Sci.* **27** 1279–87
- [20] Phelps A V 1985 JILA Information Center Report No 28
- [21] Cosby P S 1993 Electron-impact dissociation of oxygen *J. Chem. Phys.* **98** 9560–9
- [22] Klopovskiy K S, Lopaev D V, Rakhimov A T, Rakhimova T V and Smirnov A V 2002 Surface recombination of O and H atoms under the discharge conditions *Proc. 16th ESCAMPIG—5th ICRP (Grenoble, 2002)* vol 1, pp 171–2
- [23] Lopaev D V and Smirnov A V Non-equilibrium heterogeneous processes in plasma with oxygen atoms on a quartz surface: experimental results and modeling 2002 *Proc. 3rd Int. Symp. on Theoretical and Applied Plasma Chemistry 2002 (Plyos, Russia)* vol 1, pp 213–16
- [24] Klopovskiy K S, Lopaev D V, Proshina O V, Rakhimova T V and Rakhimov A T 2002 Efficiency of singlet oxygen pumping in plasma. II. The $O_2(a^1\Delta_g)$ and $O_2(b^1\Sigma_g^+)$ production in glow discharge *Proc. 16th ESCAMPIG—5th ICRP (Grenoble, 2002)* vol 2, pp 39–40
- [25] Klopovskiy K S, Lopaev D V, Popov N A, Rakhimov A T and Rakhimova T V 1999 Heterogeneous quenching of $O_2(^1\Delta_g)$ molecules in $H_2 : O_2$ mixtures *J. Phys. D: Appl. Phys.* **32** 3004–12
- [26] Nowakowska H, Zakrzewski Z and Moisan M 2001 *J. Phys. D: Appl. Phys.* **34** 1474–8
- [27] Naidis G V 2001 *J. Phys. D: Appl. Phys.* **34** L103–4
- [28] Carroll D L, Verdeyen J T, King D M, Zimmerman J W, Laystrom J K, Woodard B S, Benavides G F, Kittell K and Solomon W C 2004 Path to the measurement of positive gain on the 1315 nm transition of atomic iodine pumped by $O_2(a^1\Delta)$ produced in an electric discharge *IEEE J. Quantum Electron.* **41** 213
- [29] Carroll D L 2004 private communication